



**Facets Control Charge Separation during
Photoelectrochemical Water Oxidation with Strontium
Titanate (SrTiO₃) Single Crystals**

Journal:	<i>Energy & Environmental Science</i>
Manuscript ID	EE-ART-12-2023-004308.R1
Article Type:	Paper
Date Submitted by the Author:	11-Mar-2024
Complete List of Authors:	Assavachin, Samutr; University of California, Department of Chemistry Xiao, Chengcan; University of California, Department of Chemistry Becker, Kathleen; University of California, Department of Chemistry Osterloh, Frank ; University of California, Department of Chemistry

Broader Context Statement

In photoelectrochemical cells, charge separation is usually achieved with an applied electric potential. However, photocatalysts for the overall water splitting (OWS) reaction must be able to drive the endergonic process without an applied bias. Photochemical labelling reactions suggest that charge separation in such photocatalysts is affected by the crystal facets, which attract electrons or holes selectively. However, quantitative information on the photovoltage and junction properties of facets is difficult to find in the literature. Here we use hydrogen annealed SrTiO_{3-x} single crystals to study the facet dependence of the photoelectrochemical water oxidation reaction. We find that photovoltage and photocurrent vary among facets and that this can be attributed to work function (flat band potential) differences that control the band bending (built-in voltage) of the respective semiconductor-liquid junctions. After adjusting for donor concentrations, the (110) facets have the highest electron transfer barrier, followed by the (111) and then the (100) facets. Overall, these experiments provide the first quantitative assessment of the facet-dependent SrTiO_{3-x} junction properties and OER activities. This provides a general thermodynamic basis for photochemical charge separation in photocatalysts and helps explain the better energy conversion efficiency of faceted over non-faceted photocatalysts for the overall water splitting reaction.

Facets Control Charge Separation during Photoelectrochemical Water Oxidation with Strontium Titanate (SrTiO₃) Single Crystals

Samutr Assavachin, Chengcan Xiao, Kathleen Becker, and Frank E. Osterloh*

Abstract

5 The photocatalytic overall water splitting reaction provides a pathway to hydrogen fuel from sunlight. Photocatalysts must achieve the reaction without the application of an external bias, which requires an effective charge separation mechanism. Photolabeling studies and electrostatic simulations for the well-known CoOOH/Al:SrTiO₃/Rh/Cr₂O₃ photocatalyst suggest that charge separation is driven by work function differences at the (100) and (110) facets of SrTiO₃, which are electron and hole selective, 10 respectively. Here we use hydrogen annealed SrTiO_{3-x} single crystals to obtain the first quantitative assessment of the charge separation ability of the (100), or (110), or (111) facets during oxygen evolution. Under UV illumination (60 mW cm⁻²) the crystals exhibit variable water oxidation photocurrents (0.34, 0.82, 1.36 mA cm⁻² at 1.23 V versus RHE) and photovoltage values of 1.40, 1.52 and 1.52 V for (100), (110), and (111) SrTiO_{3-x}, respectively. A photovoltage increase in that same order 15 (0.31 V < 0.57 V < 0.67 V) is confirmed independently with vibrating Kelvin Probe Surface Photovoltage Spectroscopy (VKP-SPV) under 375 nm (1.91 mW cm⁻²) illumination. Mott Schottky measurements in aqueous K_{3/4}[Fe(CN)₆] reveal facet-dependent flatband positions of -0.58, -0.71, and -0.74 V RHE for the (100), (110), and (111) crystals respectively. This confirms that the photoelectrochemical water oxidation performance of SrTiO_{3-x} crystals is controlled by the work 20 function of each facet, which determines the barrier height of the respective solid-liquid junctions. After correcting for differences in electron donor concentrations, work function (electron transfer barriers) are found to increase in the order (100) < (111) < (110) and differ by as much as 0.16 eV, similar to an earlier prediction. Overall, these results explain the charge separation mechanism in SrTiO₃

photocatalysts and highlight the need for faceted semiconductor crystals as light absorbers in particle-based photocatalysts.

INTRODUCTION

5 The photocatalytic water splitting reaction provides a path to sustainable hydrogen fuel without the use of photovoltaic devices.¹⁻³ Because the reaction is endergonic, an effective charge separation mechanism is required to move the reaction forward and to prevent the thermodynamically favored electron-hole recombination reaction.⁴ In photoelectrochemical cells for the overall water splitting (OWS) reaction, charge carrier separation can be achieved with an applied electric bias,⁵ or via the use of solid-solid⁶ or
10 solid-liquid junctions⁷ and with charge selective contacts.⁸ In contrast, particle-based photocatalysts must be able to generate the electric potential for OWS without any external applied bias.⁹ Charge separation in these catalysts is believed to be heavily influenced by the charge carrier affinities of crystal facets. Indeed, for La:NaTaO₃¹⁰ TiO₂,¹¹ BiVO₄,^{12, 13} Bi₂WO₆,¹⁴ PbTiO₃,¹⁵ SrTiO₃,^{16, 17} BaTiO₃,¹⁸ and WO₃ crystals¹⁹ photolabeling techniques have established preferential affinities of facets for
15 photoholes and photoelectrons.²⁰ For example, Pt particles will reductively photodeposit on the (100) facet of BiVO₄, while PbO₂ will oxidatively deposit on the (110) facet, as a result of electrons and hole accumulation, respectively.¹² However, to date, quantitative measurements of the local electrochemical potential (work function) of facets in the dark or under illumination are very rare.²⁰⁻²³

The CoOOH/Al:SrTiO₃/Rh/Cr₂O₃ photocatalyst²⁴ is one of the best characterized and most efficient
20 OWS catalysts to date. It has been speculated that charge separation in this catalyst is a result of the electron affinity of the SrTiO₃ (100) facets and the hole affinity of the (110) facets, as controlled by the local work functions of the facets.¹⁷ This is supported by electrostatic simulations, which suggest that a 0.2 eV work function difference between facets is sufficient to achieve charge separation in the system.

²⁴ Additionally, kinetic simulations combined with electrochemical measurements show that charge separation in that catalyst is also influenced by the *charge transfer kinetics* of the sites for hydrogen evolution reaction (HER) and oxygen evolution reaction (OER). ²⁵ Electrons move to the HER sites (and holes to the OER sites) because of the rapid reaction of the charge carriers at these locations. This suggests that charge separation in this photocatalyst is controlled by both kinetic and thermodynamic factors. ²⁶

Here we provide the first experimental evidence that the oxygen evolution reaction (OER) with SrTiO₃ is indeed facet-dependent and controlled by the thermodynamics (work function) of each facet. For the study we select commercially available SrTiO₃ single crystals with (100, 110, 111) facets. As can be seen from **Figure 1**, these facets have different chemical compositions and structures, ²⁷ and therefore, their electrochemical potentials (work functions) are expected to vary as well. ^{28, 29} Indeed, KPFM and Low Energy Electron Microscopy measurements have observed work function variations of 0.07 eV for the charge-neutral SrO or TiO₂ terminations of the (100) facet.³⁰ However, these data are difficult to transfer to SrTiO₃-water interfaces which undergo chemical changes in water. For example, Time-Of-Flight Mass Spectrometry (TOF-MS) studies by Biswas et al. show that facets exposed to water become Ti rich after loss of soluble Sr²⁺ ions. ²⁷ Also, protonation,³¹ specific ion adsorption ³² and trapped charge carriers ³³ and oxygen vacancies ²² will further modify the work function of these surfaces and their affinity to photogenerated charge carriers. The relative contributions of these processes are difficult to evaluate theoretically, making experimental studies indispensable.

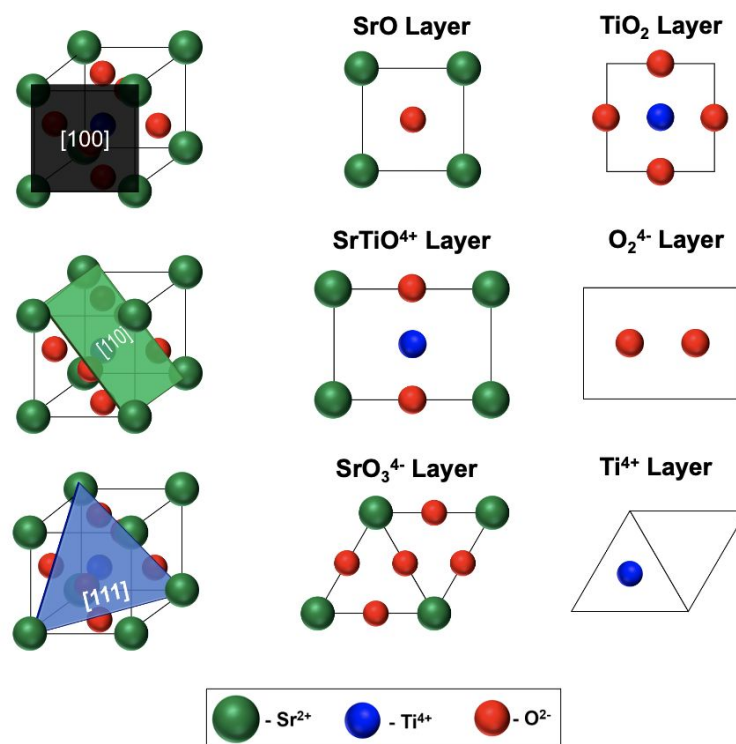


Figure 1. Facets of SrTiO₃ with different surface terminations. Top Row (100), Middle Row (110), Bottom Row (111). The (100) facets are terminated by SrO or TiO₂, respectively. The (110) facets are comprised of SrTiO₄⁺ and O₂⁴⁻ layers and the (111) facets are made of hexagonal surface structures of SrO₃⁴⁻ and Ti⁴⁺. See also Biswas et al.²⁷

In order to experimentally observe the effect of the facets on photoelectrochemical water oxidation, SrTiO₃ crystals were annealed in hydrogen,³⁴⁻³⁶ and studied with photoelectrochemical scans, surface photovoltage spectroscopy, and Mott Schottky measurements. Correcting for variations in the electron donor concentrations of the crystals, we find that the photohole selectivity increases for (100) < (111) < (110), SrTiO₃ crystals and is controlled by the work function of the facets, as determined by the flatband potential. A more reducing flatband potential leads to a larger junction barrier for electron transfer and makes hole transfer more selective. These results explain the charge separation mechanism in the efficient CoOOH/Al:SrTiO₃/Rh/Cr₂O₃ photocatalyst,²⁴ which is terminated by hole selective (110) and electron selective (100) facets. The results also explain why photocatalysts without well-formed facets,

such as SrTiO₃ *nanocrystals*,^{37, 38} have lower photocatalytic activities for endergonic reactions, such as the water splitting reaction. These insights are important for the engineering of improved photocatalysts for solar energy conversion.

5 RESULTS AND DISCUSSION

Strontium titanate (SrTiO₃) single crystals with [100, 110, 111] orientations (*MSE Supplies*, 10 x 10 x 0.5 mm) were annealed at 1,100°C in Forming gas (10% H₂ / 90% Argon) for 6 hours. SEM images after H₂ annealing are shown in (**Figure 2a-c**) and confirm a smooth and uniform surface of the crystals on the 500 μm scale. According to XRD (**Figure 2d**), the crystals retain their phase purity and (100, 110,
10 111) crystal orientations after the annealing treatment.

Optical absorption spectra of the pristine and H₂-annealed SrTiO_{3-x} single crystals are shown in **Figure 2e**. Optical bandgaps are observed at 3.2 eV (390 nm) agreeing with the literature value of 3.2 eV.³⁴ After hydrogen annealing, SrTiO_{3-x} crystals turn black (**Figure S1**) and develop a secondary absorption feature in the visible light region that extends into the infrared (IR) region. These optical changes are
15 well documented in the literature³⁴⁻³⁶ and result from excitation of free electrons in the SrTiO_{3-x} conduction band.³⁹

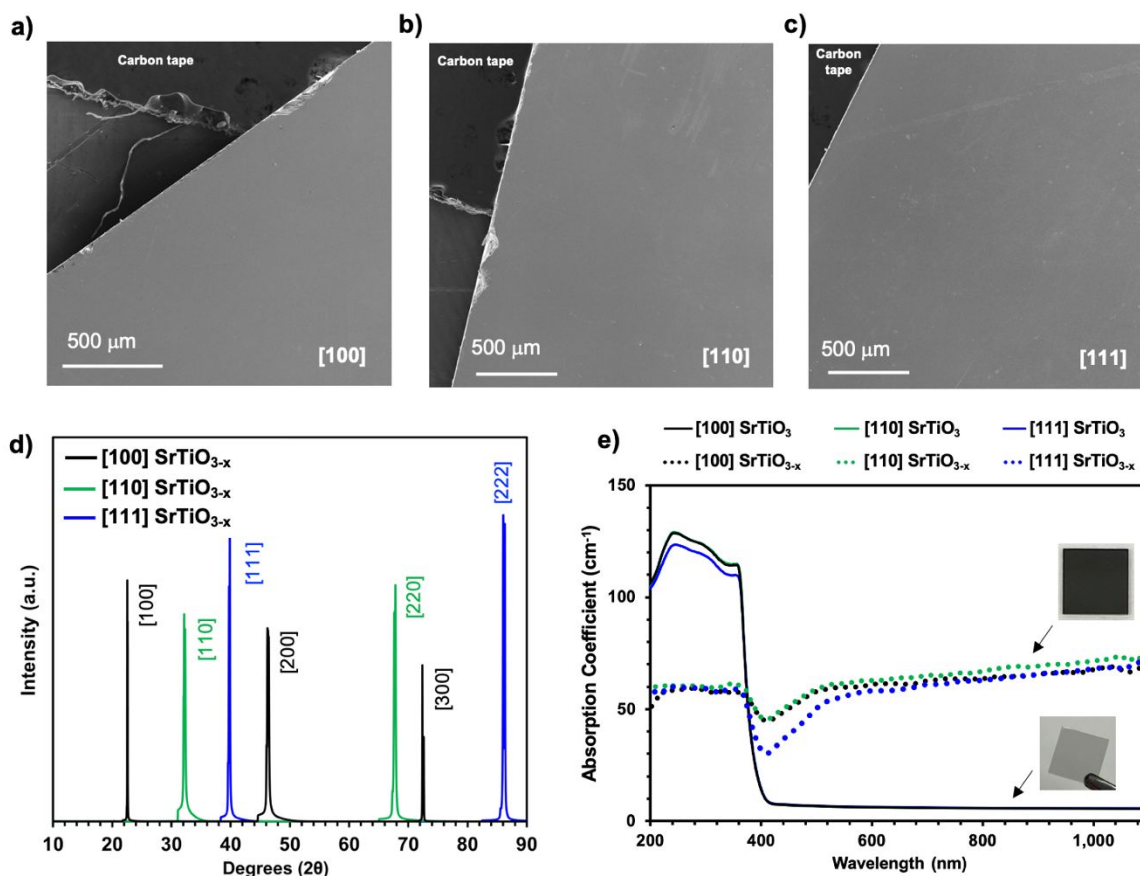


Figure 2. H₂-annealed SrTiO_{3-x} (111, 110, and 100) oriented single crystals. a-c) SEM images, d) XRD patterns, e) UV-Vis spectra of as-received and H₂-annealed samples. Inset shows photos of as-received and H₂-annealed crystals. Additional images are available in **Figure S1**.

5

X-ray photoelectron spectroscopy (XPS) was conducted to study the surface composition of (100), (110), and (111) oriented SrTiO₃ crystals pre- and post-H₂ annealing. Binding energies for all elements are summarized in **Table S1**. Survey scans (**Figure S2**) confirm the presence of Sr, Ti, and O peaks before and after H₂ annealing. For the pristine SrTiO₃ single crystals, the Sr 3d_{5/2} peak is at 132.4 - 132.7 eV, the Ti 2p_{3/2} peak at 457.8 - 458.0 eV, and the O 1s peak at 528.9 - 529.1 eV. This matches the results from previous reports.⁴⁰⁻⁴⁴ For the (100), (110), and (111) facets of SrTiO_{3-x} single crystals, Ti 2p peaks

are shifted to higher binding energy by 0.41 eV, 0.38 eV, and 0.5 eV respectively (**Figure 3a-c**). This indicates that H₂ annealing shifts the Fermi level 0.38 – 0.50 eV towards the conduction band of SrTiO₃. This agrees with the expected increased donor concentration resulting from reduction by H₂. Two additional shoulder peaks at lower energy relative to the major peaks of Ti 2p_{1/2} and Ti 2p_{3/2} were observed post H₂-annealing and are attributed to Ti³⁺ species.^{45, 46} The Ti³⁺ ions are consistent with the reduction of SrTiO₃ during H₂ treatment, however, Ti³⁺ species are sometimes not observed in the XPS of SrTiO_{3-x}, as a result of surface reactions with air or water.^{40, 45}

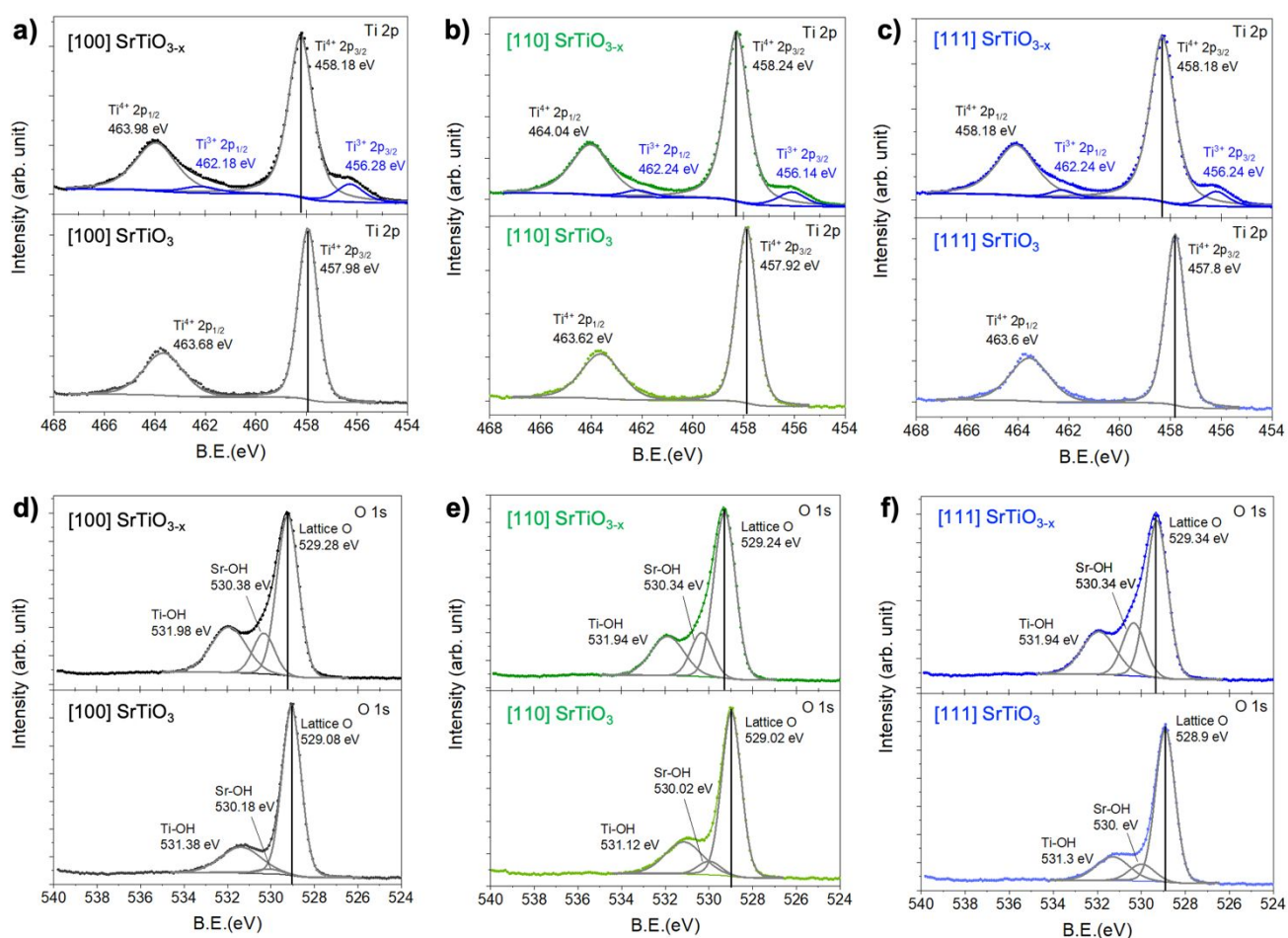


Figure 3. Ti 2p peak of a) (100), b) (110), and c) (111) facets of single crystal SrTiO₃ and O 1s peak of d) (100), e) (110), and f) (111) facets of single crystal SrTiO₃ before and after H₂ annealing. Top section is for H₂ annealed samples. Bottom section is for as-received, non-annealed samples. The position of

each fitted peak is marked with a vertical black line to show the peak shift resulted from H₂ annealing.

High resolution O 1s spectra are shown in (**Figure 3d-f**). After H₂ annealing, the O 1s lattice peaks are shifted by 0.2 eV, 0.22 eV, and 0.44 eV for the (100), (110) and (111) facets, respectively. This shift stems from the Fermi level change, as discussed before for the Ti 2p peaks. Additionally, a significant increase in the Ti-OH⁴²⁻⁴⁴ and Sr-OH⁴² peaks intensities were observed post H₂ annealing. The hydroxyls are result of the reaction of surface Ti³⁺ ions with water, according to $\text{Ti(3+)} + \text{H}_2\text{O} \rightarrow \text{Ti(4+)-OH} + \frac{1}{2} \text{H}_2$. An overlay of the six O1s spectra for the as-received and H₂-annealed samples is shown in **Figure S3a** and **b**. For each set of samples, the shape and intensity of the O shoulders from all three facets are similar, indicating no significant compositional differences for the (111), (110), and (100) facets. The binding energies for the oxygen peaks are summarized in (**Table S1**). Lastly, Sr 3d peaks were shifted by 0.14 eV, 0.27 eV, and 0.30 eV respectively (**Figure S4**) after H₂ annealing. The Sr shoulder peaks (0.7 eV higher energy than Sr 3d major peak) are assigned to surface Sr²⁺ ions bonded to hydroxide or peroxide.⁴⁷⁻⁵¹ Overall, these results confirm the conversion of SrTiO₃ into SrTiO_{3-x} during the H₂ annealing treatment.

The photoelectrochemical (PEC) activity of the H₂ annealed single crystals was observed in aqueous 0.50 M Na₂SO₄ in air under UV light illumination (60 mW cm⁻²), as seen in **Figure 4**. For the H₂ annealed crystals, the anodic photocurrent is due to water oxidation, as evidenced by the stability of the current over 4 h (74% of initial current maintained, **Figure S8**). After 4.5 hours, gas chromatography detects 30.6 micromoles of O₂ in the headspace, corresponding to a Faraday efficiency of 73.8%. The O₂ deficiency is attributed to residual O₂ dissolved in the electrolyte and to the formation of H₂O₂, as shown previously by Wrighton et al.³⁵ (111) SrTiO_{3-x} yields the highest anodic photocurrent (1.30 mA cm⁻² at 1.23 V RHE), followed by (110) SrTiO_{3-x} (0.81 mA cm⁻²) and (100) SrTiO_{3-x} (0.34 mA cm⁻²). Anodic photo-onsets (E_{on}) are similar for (111) and (110) SrTiO_{3-x} at -0.287 V vs RHE while (100) SrTiO_{3-x} exhibits the least reducing onset at -0.190 V vs RHE. These values correspond to a photovoltage

of $V_{\text{ph}} = E^0 - E_{\text{on}}$ of 1.52 V for both (111) and (110) SrTiO_{3-x} and of 1.42 V for (100) SrTiO_{3-x} electrodes (using $E^0 = 1.23$ V RHE for the $\text{O}_2/\text{H}_2\text{O}$ couple). Measurements were reproducible in three separate crystal samples, as shown in **Figure S9** and **Table S2**. The mean photocurrents for (100) SrTiO_{3-x} , (110) SrTiO_{3-x} , and (111) SrTiO_{3-x} are 0.34, 0.82, and 1.36 mA cm^{-2} (1.23 V RHE) respectively, with the highest standard deviation of 0.08 mA cm^{-2} (5.89 %) in the (111) SrTiO_{3-x} sample. Mean photocurrent onsets for three separate crystal samples were -0.294 V RHE for (111) SrTiO_{3-x} , -0.286 V RHE (110) SrTiO_{3-x} , and -0.172 V RHE for (100) SrTiO_{3-x} .

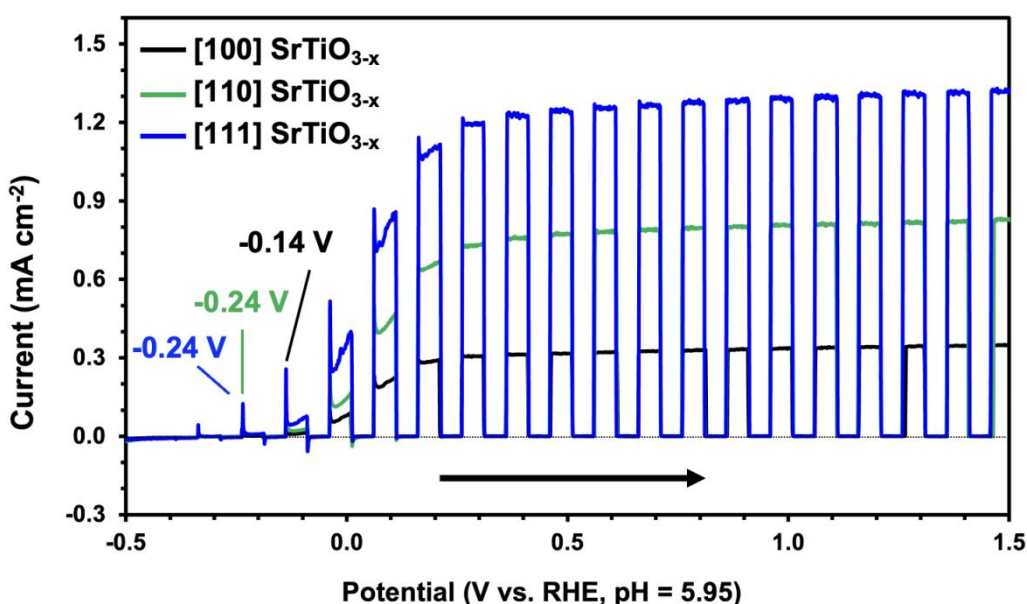


Figure 4. a) PEC scans of H_2 annealed strontium titanate single crystals under UV illumination (60 mW cm^{-2}) from Xe Lamp in 0.50 M Na_2SO_4 non-degassed aqueous solution (pH = 5.95). Single crystals were coated with InGa eutectic to establish an Ohmic contact. The scan direction is from negative to positive potential as indicated by the horizontal arrow. The active area of electrode is 0.50 cm^2 . The small reductive dark current is attributed to reduction of residual adsorbed O_2 . The measurement configuration is shown in **Figure S5a** and a close-up of the photo onset shown in **Figure S6**. For the as-purchased single crystals, no photocurrent was obtained due to the insulating property of the material (**Figure S7**).

To independently determine the photovoltage of the three crystals, Vibrating Kelvin Probe Surface Photovoltage Spectra (VK-SPS) were recorded for all samples. VKP-SPS measures the contact potential difference (CPD) change of a thin film with a commercially available vibrating Kelvin probe (Besocke Delta Phi).^{52, 53} Illumination through the semi-transparent probe produces a surface photovoltage signal $SPV = CPD_{light} - CPD_{dark}$. The sign and size of the SPV signal provides information about the bandgap, majority carrier type and photoelectrochemical reactivity of semiconductors.^{54, 55} Under certain circumstances, the SPV signal equals the photovoltage of the semiconductor-liquid contact.^{56, 57} To mimic the conditions during water oxidation, SrTiO_{3-x} crystals were brought in contact with ~8 μ L of 0.50 M aqueous Na₂SO₄, covered with a microscopy cover slip glass and placed inside of measurement chamber purged continuously with H₂O saturated O₂. The sample configuration is shown in **Figure S11** and resulting spectra are shown in **Figure 5a**. The major photovoltage signal onset occurs at 2.9 eV, slightly below the optical band gap of the material (3.2 eV). Additionally, a sub-band gap signal is observed at 2.05 eV, which is attributed to the excitation of Ti³⁺ defect states, as described before.^{46, 58} At ~3.3 eV (375 nm) the maximum Δ CPD varies from -0.67 V for (111) SrTiO_{3-x} to -0.57 V for (110) SrTiO_{3-x} and -0.31 V for (100) SrTiO_{3-x}. These surface photovoltage signals are smaller than the photovoltage values from PEC due to the lower light intensity in the SPV measurement (1.91 mW cm⁻² at 375 nm), but the trend agrees well with the PEC measurements in **Figure 4**. This confirms that the facets differ in their ability to generate a photovoltage, and that this controls the photocurrent in **Figure 4**.

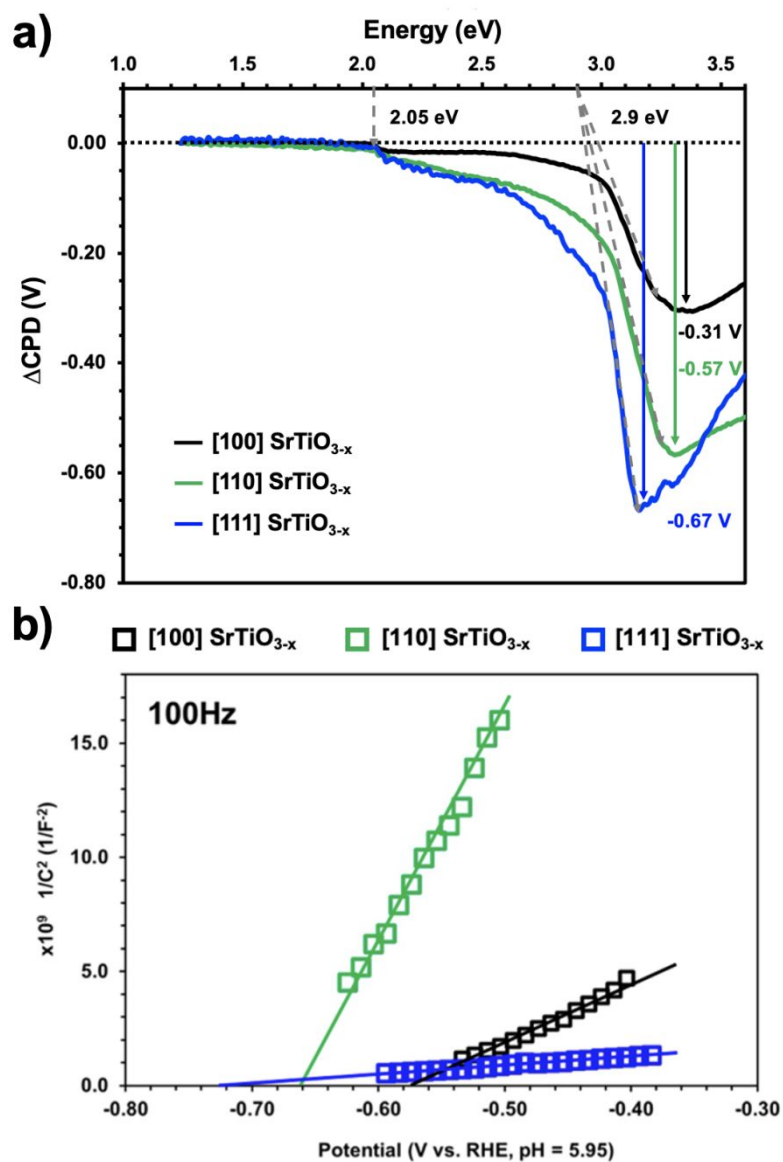


Figure 5. a) Surface photovoltage spectra of SrTiO_{3-x} single crystals exposed to 0.50 M Na_2SO_4 aqueous electrolyte in a H_2O -saturated oxygen gas atmosphere. Illumination was provided by a 300 W Xe light source and filtered through a monochromator to yield an irradiance of 1.91 mW cm^{-2} at 3.3 eV. The scan direction was from low to high energy. b) Mott Schottky plots at 100 Hz in 0.50 M Na_2SO_4 aqueous solution (pH = 5.95) with 50 mM equimolar $\text{K}_{3/4}[\text{Fe}(\text{CN})_6]$ under constant nitrogen purging without illumination. Crystals were contacted electrically with InGa eutectic, as shown in **Figure S5b**. Additional data is presented in **Figure S12** and **Table S3**.

To determine the reason for the photovoltage difference, the flatband potentials of the three SrTiO_{3-x} liquid interfaces were measured using the Mott-Schottky (MS) technique at frequencies of 100, 125, and 150 Hz. The flatband potential E_{FB} is the potential required to flatten the bands (remove the depletion layer) at the semiconductor-electrolyte junction, as shown in **Figure 6**. This occurs when the applied potential equals the workfunction of the facets at the electrolyte interface. To ensure a well-defined depletion layer, the fast K_{3/4}[Fe(CN)₆] redox couple (50 mM each) was added into 0.50 M Na₂SO₄ aqueous solution and oxygen was removed by purging with nitrogen gas for 30 minutes before and throughout the experiment. As can be seen in **Figures 5b** and **S12**, MS plots are linear for all the frequencies tests and have a positive slope consistent with the formation of an electron depletion region. From the MS slopes, the excess electron density, N_{D} , can be calculated using the parameters in **Table S3**. Mean N_{D} values (from all MS slopes in **Figure S12**) are 5.14×10^{18} , 2.14×10^{19} , and 1.26×10^{20} cm⁻³ for (110), (100), and (111), and SrTiO_{3-x} respectively. Considering that the same annealing conditions were used for all crystals, the observed difference in free electron density may be due to differences in O²⁻ and electron transport along [111], [110], and [100] directions. The good agreement between the trend in donor concentrations with the trend in water oxidation photocurrents at 1.23 V vs RHE (**Figure 4**) shows that photocurrents in the kinetic regime (at large driving force) are controlled by the donor concentrations of the samples and their conductivity.

From the x-intercept of the Mott Schottky (MS) plots, the flatband potentials (E_{FB}) can be obtained. They vary in the order (100) SrTiO_{3-x} (-0.58 V vs RHE) > (110) SrTiO_{3-x} (-0.71 V) > (111) SrTiO_{3-x} (-0.74 V), as shown in **Table 1** and in the energy diagram in **Figure 6**. The more reducing flatband potential for the (111) facet results in a higher the built-in voltage of the SrTiO_{3-x}/electrolyte contact, and a higher electron transfer barrier. That explains the larger photovoltage for the (111) crystals. **Figure 6** also reveals the important effect of the donor concentration N_{D} on the flatband potential. The higher N_{D} , the more reducing E_{FB} , and the larger V_{Bi} . The ability to control V_{Bi} with the donor concentration is one way

to achieve junctions with improved photocarrier separation.^{8, 59-62}

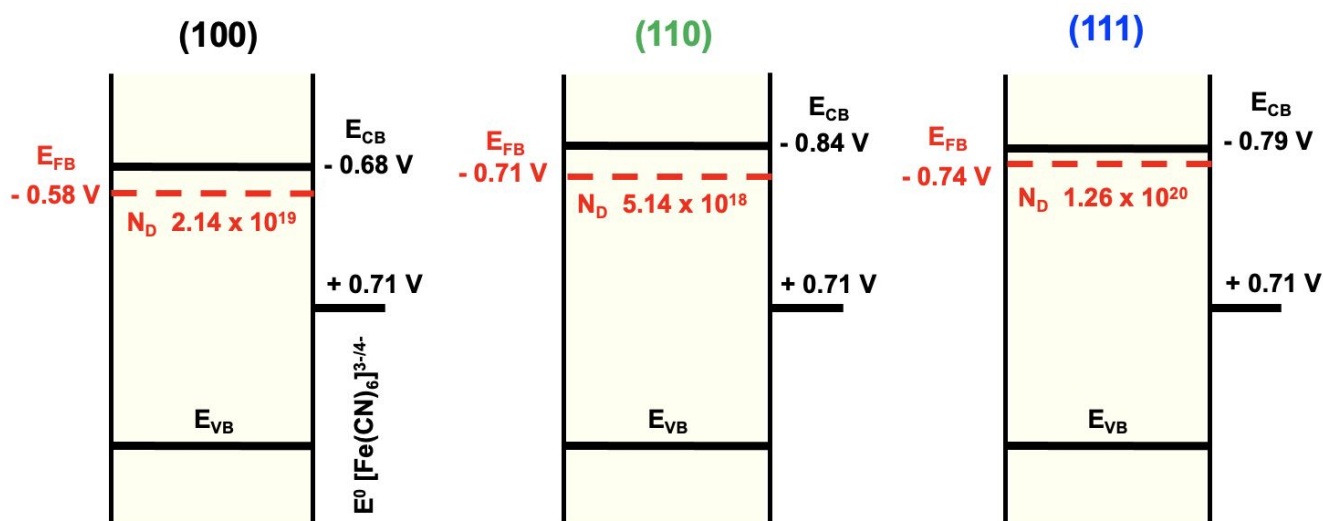


Figure 6. Energy diagrams for (100) SrTiO_{3-x} (left), (110) SrTiO_{3-x} (middle), (111) SrTiO_{3-x} (right) in contact with hexacyanoferrate electrolyte in the dark. Values for the flatband potential (E_{FB}), the conduction band edge (E_{CB}), the donor concentrations (N_D), and the $[\text{Fe}(\text{CN})_6]^{3-/4-}$ standard reduction potential (E^0) are also shown. For details see **Tables 1 and S3**.

However, in order to determine the *intrinsic charge selectivity* of each crystal it is important to have at a N_D -independent description of the built-in voltage. That can be achieved by calculating the conduction band edge for each crystal from N_D and from the known effective density of states using the Nernst equation (details in **Table S3**). These adjusted band edge values are also shown in **Figure 6**. Interestingly, the (110) crystals are now revealed to have the most reducing E_{CB} , followed by the (111) and then (the 100) crystals. That means that if donor concentrations N_D were equal across the series, the work functions of the crystals would vary in the order of (110) > (111) > (100), and so would their built-in voltages in O₂/water.

Table 1. Values for photocurrent, flatband potentials, built-in potentials, surface photovoltage, and conduction band edges for three facets of SrTiO_{3-x}. More details in **Table S3**.

	(100) SrTiO _{3-x}	(110) SrTiO _{3-x}	(111) SrTiO _{3-x}
Photocurrent at 1.23 V RHE / mA cm ⁻²	0.34 ± 0.01	0.82 ± 0.00	1.36 ± 0.08
Photovoltage V _{Ph} (from PEC) / V	1.40 ± 0.03	1.52 ± 0.05	1.52 ± 0.01
Surface photovoltage SPV / V	0.31	0.57	0.67
Flatband potential E _{FB} (average from MS) / V RHE	-0.58 ± 0.02	-0.71 ± 0.017	-0.74 ± 0.007
Donor density N _D / cm ⁻³	2.14 × 10 ¹⁹	5.14 × 10 ¹⁸	1.26 × 10 ²⁰
Built-in potential V _{bi} [E _{FB} - E ⁰ (O ₂ /H ₂ O)] / V	1.81	1.94	1.97
Conduction Band Edge E _{CB} / V vs RHE at pH = 5.95	-0.68 ± 0.02	-0.84 ± 0.02	-0.79 ± 0.01
Depletion Layer width w / nm	53.2 ± 5	111 ± 3	22.6 ± 0.4

Figure 7 depicts the predicted behavior of a set of SrTiO_{3-x} crystals with equal donor concentrations under photoelectrochemical water oxidation conditions. Excitation generates charge carriers that are separated by the junctions at the SrTiO_{3-x}/liquid interface. The more reducing E_{CB}, the larger the electrostatic barrier V_{Bi} for electron transfer into the solution. Accordingly, the electron-hole separation increases in the order of (100) < (111) < (110) facets. This agrees with the earlier predictions for SrTiO₃ single crystals on the basis of photolabeling experiments, which showed that electrons move to the (100) facets and holes to the (110) facets^{16, 17} The experimental built-in voltage difference between (100) and (110) facets of 0.16 V is in close agreement with the 0.20 V estimate from electrostatic simulations for the CoOOH/Al:SrTiO₃/Rh/Cr₂O₃ photocatalyst (see introduction).²⁴ This confirms that the work

function differences of the SrTiO₃ facets drive photoelectrochemical charge separation in this system and in related photocatalyst preparations that do not contain a OER cocatalyst.^{9, 46, 63} Furthermore, the findings provide an explanation for the low water splitting performance of nanoparticulate Al:SrTiO₃ photocatalysts (0.06% AQE at 375 nm),³⁸ which, due to their small size, lack well-formed facets to drive charge separation.”

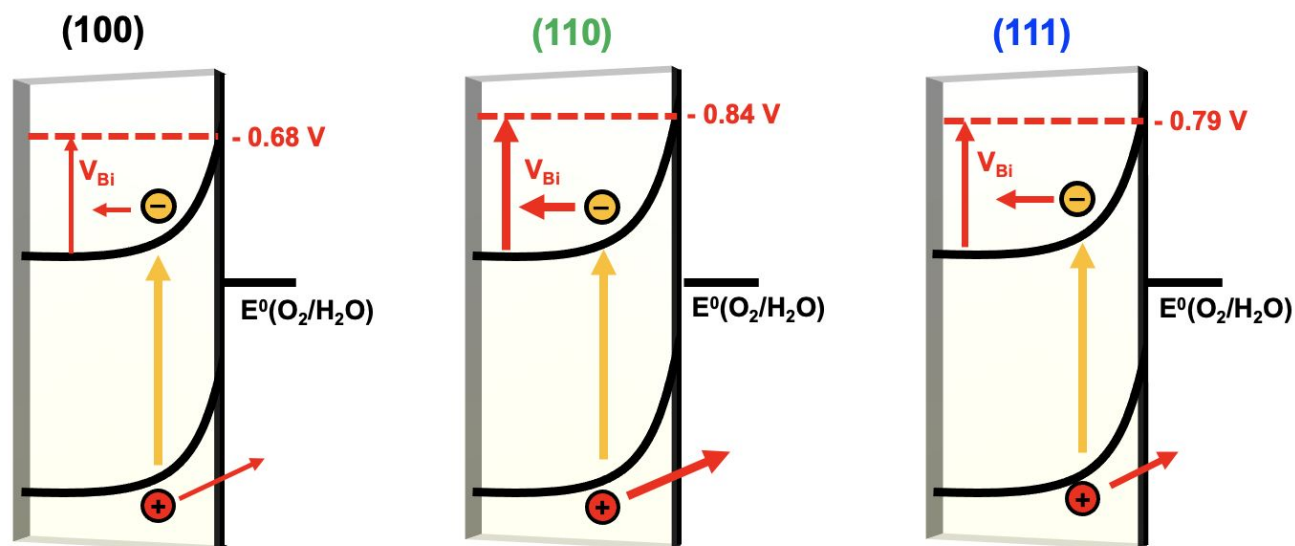


Figure 7. Energy diagrams for (100) SrTiO_{3-x} (left), (110) SrTiO_{3-x} (middle), (111) SrTiO_{3-x} (right) at equal donor concentration in contact with O₂/H₂O under illumination. Under these conditions, the potential drop in the depletion layer (the built-in voltage V_{bi}) increases in the order (100) < (111) < (110). Data in **Table 1**.

Additionally, the data in **Table 1** allows calculation of the depletion layer thickness w for each crystal in contact with a O₂ saturated H₂O solution. Values range from 22.6 nm for (111) SrTiO_{3-x} to 53 nm for the (100) SrTiO_{3-x} and to 111 nm for the (110) SrTiO_{3-x} crystal and are controlled mainly by the donor concentration N_D of each sample. Comparison with the PEC data shows that the depletion layer thickness w does not control the OER performance of the crystals. Rather, the different flatband potentials (work functions at the interface) derived from the Mott-Schottky data are the reason for the observed

differences in water oxidation. This corroborates the PEC and SPV data of the SrTiO_{3-x} crystals measured here, and it explains the charge separation mechanism in faceted SrTiO₃ photocatalysts.

CONCLUSION

5 In conclusion, hydrogen annealing of strontium titanate single crystals with (100, 110, 111) orientations at 1,100°C yields SrTiO_{3-x} crystals whose photoelectrochemical water oxidation activity under UV light illumination exhibits significant variations, with (111) faceted SrTiO_{3-x} crystals demonstrating the highest photocurrent and photovoltage followed by (110) SrTiO_{3-x} and then (100) SrTiO_{3-x}. Photovoltage values under UV illumination (60 mW cm⁻²) increase from 1.42 V for (100) SrTiO_{3-x} to 1.52 V for (111) 10 and (110) SrTiO_{3-x}, in reasonable agreement with the trend in surface photovoltage values (0.31 V, 0.57 V, 0.67 V) for (100), (110), and (111) SrTiO_{3-x} respectively, under 3.75 nm (1.92 mW cm⁻²) illumination. According to Mott Schottky (MS) measurements in hexacyanoferrate(3-/4-) solution, the (111) SrTiO_{3-x} crystals have the most reducing flatband potential E_{FB} of (-0.74 V RHE), followed by the (110) SrTiO_{3-x} crystals (-0.71 RHE), and then the (100) SrTiO_{3-x} crystals (-0.58 V RHE). This means band bending 15 increases in the series (100) SrTiO_{3-x} < (110) SrTiO_{3-x} < (111) SrTiO_{3-x}, which explains the observed OER reactivity trend. Using the donor densities obtained from the MS data, conduction band edges, E_{CB}, can be calculated for the three crystals. Here (100) SrTiO_{3-x} has the most oxidizing conduction band position (-0.68 V) while (111) SrTiO_{3-x} and (110) SrTiO_{3-x} have values of -0.79 V and -0.84 V, respectively. That means that at equal donor density, the (110) SrTiO_{3-x} surface is expected to form the 20 best junction (strongest band bending) with the O₂/H₂O redox couple, followed by (111) SrTiO_{3-x}, and (100) SrTiO_{3-x}. This confirms earlier photolabeling results by the Can Li¹⁷ and Domen groups,²⁴ which indicated the (110) facets of SrTiO₃ to be most suitable for hole accumulation and the (100) facets of SrTiO₃ most suitable for electron accumulation. Also, the measured work function difference of 0.16 eV

between (110) and (100) facets compare well to the previous estimate of 0.20 eV. Overall, these experiments provide the first quantitative assessment of the facet-dependent SrTiO_{3-x} junction properties and their OER performance. The greater the workfunction of a facet, the larger the built-in potential (band bending), and the better the charge separation ability of the junction. This provides a thermodynamic basis for photochemical charge separation in SrTiO₃-based and other photocatalysts. It also explains the better energy conversion efficiency of well crystallized photocatalysts, which can guide charge carriers to different surface facets. Photocatalysts without facets, on the other hand, allow electrons and holes to reach the same surface sites, leading to e/h recombination and energy loss.

10 EXPERIMENTAL SECTION

Water was purified to 18 MΩcm resistivity using a nano-pure system. Double polished single crystals (10 x 10 x 0.5 mm) of strontium titanate with 100, 110, 111-exposed facets were purchased from *MSE Supplies*. Sodium sulfate (99.5%, Sigma Aldrich), potassium hexacyanoferrate (II) trihydrate (98.5%-102.0%, Sigma-Aldrich), potassium ferricyanide (III) (99.9%, Fischer Chemical – Fischer Scientific), gallium-indium eutectic, InGa (≥99.99% trace metal basis, Aldrich Chemistry), and anhydrous methanol (99.9%, Alfa Aesar) were used as received.

Hydrogen Reduced Strontium Titanate Annealing – SrTiO_{3-x}

As-purchased SrTiO₃ crystals were annealed in a tube furnace by placing them into a ceramic boat inside of a quartz tube, and by exposing them to 10% H₂: 90% argon (0.1 L min⁻¹ : 0.9 L min⁻¹) gas flow. Then temperature was increased to 1,100°C at a rate of 50°C min⁻¹ temperature was kept at 1,100°C for 6 hours. After that the crystals were cooled to room temperature rapidly by opening the

furnace while 10% H₂: 90% Argon continued to flow through the quartz tube. Small holes were drilled into the ceramic crucible promote gas flow. The obtained SrTiO_{3-x} crystal had a shiny black appearance (**Figure S1**).

Optical Absorption

5 A Thermo Scientific Evolution 220 Spectrometer equipped with an integrating sphere was used to measure transmittance from 200 – 1,100 nm with 2 nm increment. Transmittance was converted to absorbance where: Absorbance = 2 – log (%Transmittance). Optical absorption coefficients, α (cm⁻¹), were calculated as follows equation: $\alpha = 2.303 \times A/d$ where A is the absorbance and d is the thickness in cm. In this case, the thickness is 0.05 cm.

10 *X-ray Photoelectron Spectroscopy*

XPS measurements were conducted by Chengcan Xiao with a Supra XPS spectrometer using an Al K α source that generate x-ray at 1,487 eV and using an ultra-high vacuum (UHV) analytical chamber with a pressure of 10⁻⁷ mbar. The spectra were electrostatically corrected based on the position of C 1s (284.6 eV). SrTiO₃ single crystal pristine as bought or after H₂-annealed were surveyed for O 1s, Ti 2p, Sr 3d,
15 and survey spectrum scan. Baseline simulation of the core-level spectrum was done using the Shirley method. The area ratio between the subpeaks in each doublet was set as ratio between 2j + 1, where j is the total angular momentum quantum number. The FWHM of the subpeaks in each doublet was set equal (except for Ti 2p).

Electrochemical Measurements

20 Electrochemical measurements were conducted using a Gamry Reference 600 Potentiostat connected to a three-electrode system consisting of a platinum counter electrode and a calomel reference electrode (3.5 M KCl). The working electrode consists of a SrTiO_{3-x} single crystal mounted on a stainless steel

alligator clip via InGa eutectic to establish an ohmic contact (**Figure S5a**). Chopped light linear sweep voltammetry was accomplished in 0.50 M Na₂SO₄ aqueous electrolyte solution (pH = 5.95) in a quartz three-neck flask. UV-light illumination was from a 300 W Xe lamp source at an intensity of 60 mW cm⁻², as measured with GaAsP photodetector, in the 250-680 nm window. The system was not degassed and contains ambient amounts of air. The electrode area in contact with solution is 1.0 cm² (0.50 cm² from the front side and 0.50 cm² from the back side). Illumination occurs on the front side and the active area of the electrode for photocurrent calculation is 0.50 cm². The chopped light scan alternates between light on and light off at a 5-second interval with scan rate of 10 mV/s and scan step of 1 mV. The applied potential was adjusted from V vs. SCE to V vs. NHE by adding the difference between the half wave potential for the K_{3/4}[Fe(CN)₆] redox couple versus SCE to the redox potential at NHE (0.36 V vs. NHE). Electrical Impedance Spectroscopy (EIS) and Mott-Schottky data were measured in a sealed three-neck flask using a 50 mM equimolar K_{3/4}[Fe(CN)₆] in 0.50 M Na₂SO₄ aqueous solution (as shown in **Figure S5b**). The solution was purged with N₂ for 30 min and bubbled with N₂ throughout the measurement. InGa eutectic was applied at the working electrode between the alligator clip contact to the SrTiO_{3-x} single crystal to establish an Ohmic contact. The single crystal contact area to the electrolyte is 1.0 cm², which includes 0.50 cm² from the front side and 0.50 cm² on the back side. The EIS experiment was conducted at 100 mV rms AC voltage using 10 points/decade, with an initial frequency of 100,000 Hz and final frequency of 0.1 Hz.

Surface Photovoltage Spectroscopy

SPS measurements were accomplished by Kathleen Becker using a vibrating gold mesh Kelvin probe (Delta PHI Besocke) mounted inside a steel chamber, as shown in **Figure S11**. Deionized water (8 μL) was added to the surface of SrTiO_{3-x} single crystal and covered with a glass slide to prevent direct contact between the gold kelvin probe and the liquid solution. O₂ gas was flowed at a rate of 1.0 L min⁻¹ through two water baths before reaching the SPS chamber. The O₂ gas was allowed to fill and purge the chamber

for 15 minutes prior to the measurement. The SrTiO_{3-x} crystals are illuminated with monochromatic light in the 1.2 – 4.1 eV range using a 300 W Xe lamp filtered by a monochromator (Oriel Cornerstone 130, 1-10 $\text{mW}\cdot\text{cm}^{-2}$). The lamp intensity was measured using a silicon thermopile detector at 3.3 eV and was found to be $1.91\text{ mW}\cdot\text{cm}^{-2}$. Samples were left to equilibrate under $10,000\text{ cm}^{-1}$ illumination from the
5 monochromator until a stable baseline was obtained. Spectrum were acquired from $10,000 - 40,000\text{ cm}^{-1}$ with a measurement interval of 5 seconds and a 100 cm^{-1} illumination increment.

AUTHOR CONTRIBUTIONS

The experiments were designed by F.E.O and S.A and conducted by S.A, K.B, and C.X. The
10 manuscript was written by F.E.O. and S.A. with contributions by C.X. All authors have given approval to the final version of the manuscript.

CONFLICTS OF INTEREST

There are no conflicts of interest to declare.

15

ACKNOWLEDGEMENT

We thank the National Science Foundation (CHE 1900136) for supporting this work. Surface Photovoltage measurements were supported by a grant from the U.S. Department of Energy, Office of
20 Science, Office of Basic Energy Sciences under Award Number DOE-SC0015329. The Kratos Supra XPS instrument was funded through the US National Science Foundation under award DMR-1828238.

Electronic supplementary information (ESI) available: Photos, XPS data, diagrams, photoelectrochemical information, semiconductor data, and calculation details.

References

1. S. Nishioka, F. E. Osterloh, X. Wang, T. E. Mallouk and K. Maeda, *Nature Reviews Methods Primers*, 2023, **3**, 42.
2. Q. Wang and K. Domen, *Chem. Rev.*, 2020, **120**, 919-985.
3. K. Takanahe, *ACS Catalysis*, 2017, **7**, 8006-8022.
4. F. E. Osterloh, *ACS Energy Letters*, 2017, DOI: 10.1021/acseenergylett.6b00665, 445-453.
5. R. Krol, in *Photoelectrochemical Hydrogen Production*, eds. R. van de Krol and M. Grätzel, Springer US, 2012, vol. 102, ch. 3, pp. 69-117.
6. W. Shockley, *Bell System Technical Journal*, 1949, **28**, 435-489.
7. S. R. Morrison, *Electrochemistry at semiconductor and oxidized metal electrodes*, Plenum Press, New York, 1980.
8. U. Würfel, A. Cuevas and P. Würfel, *IEEE Journal of Photovoltaics*, 2015, **5**, 461-469.
9. G. Askarova, C. Xiao, K. Barman, X. Wang, L. Zhang, F. E. Osterloh and M. V. Mirkin, *J. Am. Chem. Soc.*, 2023, **145**, 6526-6534.
10. H. Kato, K. Asakura and A. Kudo, *J. Am. Chem. Soc.*, 2003, **125**, 3082-3089.
11. T. Ohno, K. Sarukawa and M. Matsumura, *New Journal of Chemistry*, 2002, **26**, 1167-1170.
12. R. Li, F. Zhang, D. Wang, J. Yang, M. Li, J. Zhu, X. Zhou, H. Han and C. Li, *Nat. Commun.*, 2013, **4**, 1432.
13. H. L. Tan, A. Suyanto, A. T. D. Denko, W. H. Saputera, R. Amal, F. E. Osterloh and Y. H. Ng, *Particle & Particle Systems Characterization*, 2017, **34**, 1600290.
14. A. Adenle, H. Zhou, X. Tao, Y. Zhao, M. Shi, B. Zeng, J. Qu, R. Li and C. Li, *Chem. Commun.*, 2021, **57**, 11637-11640.
15. C. Zhen, J. C. Yu, G. Liu and H.-M. Cheng, *Chem. Commun.*, 2014, **50**, 10416-10419.
16. L. Mu, B. Zeng, X. Tao, Y. Zhao and C. Li, *J. Phys. Chem. Lett.*, 2019, **10**, 1212-1216.

17. L. Mu, Y. Zhao, A. Li, S. Wang, Z. Wang, J. Yang, Y. Wang, T. Liu, R. Chen, J. Zhu, F. Fan, R. Li and C. Li, *Energ. & Environ. Sci.*, 2016, **9**, 2463-2469.
18. S. Assavachin and F. E. Osterloh, *J. Am. Chem. Soc.*, 2023, **145**, 18825-18833.
19. Y. P. Xie, G. Liu, L. Yin and H.-M. Cheng, *Journal of Materials Chemistry*, 2012, **22**, 6746-
5 6751.
20. G. Liu, J. C. Yu, G. Q. Lu and H.-M. Cheng, *Chem. Commun.*, 2011, **47**, 6763-6783.
21. M. Shen, A. J. Kaufman, J. Huang, C. Price and S. W. Boettcher, *Nano Lett.*, 2022, **22**, 9493-
9499.
22. S. Kashiwaya, T. Toupance, A. Klein and W. Jaegermann, *Advanced Energy Materials*, 2018,
10 **8**, 1802195.
23. Y. Liu, B. R. Wygant, K. Kawashima, O. Mabayoje, T. E. Hong, S.-G. Lee, J. Lin, J.-H. Kim,
K. Yubuta, W. Li, J. Li and C. B. Mullins, *Applied Catalysis B: Environmental*, 2019, **245**,
227-239.
24. T. Takata, J. Jiang, Y. Sakata, M. Nakabayashi, N. Shibata, V. Nandal, K. Seki, T. Hisatomi
15 and K. Domen, *Nature*, 2020, **581**, 411-414.
25. Z. Pan, R. Yanagi, Q. Wang, X. Shen, Q. Zhu, Y. Xue, J. A. Röhr, T. Hisatomi, K. Domen and
S. Hu, *Energ. & Environ. Sci.*, 2020, **13**, 162-173.
26. R. Yanagi, T. Zhao, D. Solanki, Z. Pan and S. Hu, *ACS Energy Letters*, 2022, **7**, 432-452.
27. A. Biswas, P. B. Rossen, C.-H. Yang, W. Siemons, M.-H. Jung, I. K. Yang, R. Ramesh and Y.
20 H. Jeong, *Applied Physics Letters*, 2011, **98**.
28. M. A. Butler and D. S. Ginley, *Journal of the Electrochemical Society*, 1978, **125**, 228-232.
29. Y. Xu and M. A. A. Schoonen, *American Mineralogist*, 2000, **85**, 543-556.
30. L. Aballe, S. Matencio, M. Foerster, E. Barrena, F. Sánchez, J. Fontcuberta and C. Ocal,
Chemistry of Materials, 2015, **27**, 6198-6204.

31. V. Chakrapani, K. Tvrđy and P. V. Kamat, *Journal of the American Chemical Society*, 2010, **132**, 1228-1229.
32. R. L. Chamousis and F. E. Osterloh, *Energ. & Envi. Sci.*, 2014, **7**, 736-743.
33. K. W. Frese, *Journal of the Electrochemical Society*, 1983, **130**, 28-33.
34. J. G. Mavroides, J. A. Kafalas and D. F. Kolesar, *Appl. Phys. Lett.*, 1976, **28**, 241-243.
35. M. S. Wrighton, A. B. Ellis, P. T. Wolczanski, D. L. Morse, H. B. Abrahamson and D. S. Ginley, *J. Am. Chem. Soc.*, 1976, **98**, 2774-2779.
36. A. Kumar, P. G. Santangelo and N. S. Lewis, *Journal of Physical Chemistry*, 1992, **96**, 834-842.
37. A. N. Adeyemi, A. Venkatesh, C. Xiao, Z. Zhao, Y. Li, T. Cox, D. Jing, A. J. Rossini, F. E. Osterloh and J. V. Zaikina, *Materials Advances*, 2022, **3**, 4736-4747.
38. Z. Zhao, E. J. Willard, H. Li, Z. Wu, R. H. R. Castro and F. E. Osterloh, *Journal of Materials Chemistry A*, 2018, **6**, 16170-16176.
39. R. L. Wild, E. M. Rockar and J. C. Smith, *Phys. Rev. B*, 1973, **8**, 3828-3835.
40. K. Xie, N. Umezawa, N. Zhang, P. Reunchan, Y. Zhang and J. Ye, *Energ. & Environ. Sci.*, 2011, **4**, 4211-4219.
41. C. Wang, P. Koirala, P. Stair and L. Marks, *Applied Surface Science*, 2017, **422**, 661-665.
42. D. Hrabovsky, B. Berini, A. Fouchet, D. Aureau, N. Keller, A. Etcheberry and Y. Dumont, *Applied Surface Science*, 2016, **367**, 307-311.
43. R. P. Vasquez, *Surf. Sci. Spectra*, 1992, **1**, 129-135.
44. H. Chen, F. Zhang, W. Zhang, Y. Du and G. Li, *Applied Physics Letters*, 2018, **112**.
45. Y. Fu, H. Du, S. Zhang and W. Huang, *Materials Science and Engineering: A*, 2005, **403**, 25-31.
46. Z. Zhao, R. V. Goncalves, S. K. Barman, E. J. Willard, E. Byle, R. Perry, Z. Wu, M. N. Huda, A. J. Moulé and F. E. Osterloh, *Energy & Environmental Science*, 2019, **12**, 1385-1395.

47. J.-Y. Baek, L. T. Duy, S. Y. Lee and H. Seo, *Journal of Materials Science & Technology*, 2020, **42**, 28-37.
48. X. Wang, K. Huang, J. Qian, Y. Cong, C. Ge and S. Feng, *Science Bulletin*, 2017, **62**, 658-664.
49. E. J. Crumlin, E. Mutoro, Z. Liu, M. E. Grass, M. D. Biegalski, Y.-L. Lee, D. Morgan, H. M. Christen, H. Bluhm and Y. Shao-Horn, *Energ. & Environ. Sci.*, 2012, **5**, 6081-6088.
50. V. Young and T. Otagawa, *Applications of Surface Science*, 1985, **20**, 228-248.
51. X. Liu, Y. Cao, B. Pal, S. Middey, M. Kareev, Y. Choi, P. Shafer, D. Haskel, E. Arenholz and J. Chakhalian, *Physical Review Materials*, 2017, **1**, 075004.
52. T. Dittrich and S. Fengler, *Surface Photovoltage Analysis of Photoactive Materials*, World Scientific Publishing Europe Ltd., London, 2020.
53. L. Kronik and Y. Shapira, *Surf. Sci. Rep.*, 1999, **37**, 1-206.
54. J. Wang, J. Zhao and F. E. Osterloh, *Energ. & Envi. Sci.*, 2015, **8**, 2970-2976.
55. J. Zhao and F. E. Osterloh, *J. Phys. Chem. Lett*, 2014, **5**, 782-786.
56. S. Daemi, A. Kundmann, P. Cendula, K. Becker and F. E. Osterloh, *Energy Environ. Sci.*, 2023, **16**, 4530-4538.
57. Y. Cheng, C. Xiao, B. Mahmoudi, R. Scheer, A. W. Maijenburg and F. E. Osterloh, *EES Catalysis*, 2023, **1**, 74-83.
58. X. Ma, Z. Wu, E. J. Roberts, R. Han, G. Rao, Z. Zhao, M. Lamothe, X. Cui, R. D. Britt and F. E. Osterloh, *The Journal of Physical Chemistry C*, 2019, **123**, 25081-25090.
59. F. A. Chowdhury, M. L. Trudeau, H. Guo and Z. T. Mi, *Nat. Commun.*, 2018, **9**.
60. M. R. Shaner, K. T. Fountaine, S. Ardo, R. H. Coridan, H. A. Atwater and N. S. Lewis, *Energ. & Environ. Sci.*, 2014, **7**, 779-790.
61. A. Cuevas and D. Yan, *IEEE Journal of Photovoltaics*, 2013, **3**, 916-923.
62. F. F. Abdi, L. H. Han, A. H. M. Smets, M. Zeman, B. Dam and R. van de Krol, *Nat. Commun.*, 2013, **4**, 2195.

63. Y. Ham, T. Hisatomi, Y. Goto, Y. Moriya, Y. Sakata, A. Yamakata, J. Kubota and K. Domen, *J. Mater. Chem. A*, 2016, **4**, 3027-3033.